Strotos, G., Gavaises, M., Theodorakakos, A. & Bergeles, G. (2011). Numerical investigation of the evaporation of two-component droplets. Fuel, 90(4), pp. 1492-1507. doi: 10.1016/j.fuel.2011.01.017

CITY UNIVERSITY LONDON

EST 1894

City Research Online

Numerical investigation of the evaporation of two component droplets

George Strotos*[1], Manolis Gavaises°,[§], Andreas Theodorakakos[+] , George Bergeles*

*National Technical University of Athens, Department of Mechanical Engineering

5 Heroon Polytechniou, 15710 Zografos, Athens, Greece

°City University London, School of Engineering and Mathematical Sciences

Northampton Square, EC1V 0HB, London, UK

[+]Fluid Research Co. 49 Laskareos Str, 11472, Athens, Greece

[§]Correspondence author email: m.gavaises@city.ac.uk

ABSTRACT

A numerical model for the complete thermo-fluid-dynamic and phase-change transport processes of two-component hydrocarbon liquid droplets consisting of n-heptane, n-decane and mixture of the two in various compositions is presented and validated against experimental data. The Navier-Stokes equations are solved numerically together with the VOF methodology for tracking the droplet interface, using an adaptive local grid refinement technique. The energy and concentration equations inside the liquid and the gaseous phases for both liquid species and their vapor components are additionally solved, coupled together with a model predicting the local vaporization rate at the cells forming the interface between the liquid and the surrounding gas. The model is validated against experimental data available for droplets suspended on a small diameter pipe in a hot air environment under convective flow conditions; these refer to droplet's surface temperature and size regression with time. An extended investigation of the flow field is presented along with the temperature and concentration fields. The equilibrium position of droplets is estimated together with the deformation process of the droplet. Finally, extensive parametric studies are presented revealing the nature of multi component droplet evaporation on the details of the flow, the temperature and concentration fields.

[1]Currently at Technological Education Institute of Piraeus, Mechanical Engineering Department, Fluid Mechanics Laboratory, 250 Thivon & P. Ralli str., Aegaleo, 12244, Greece

1   INTRODUCTION

Droplet evaporation is an important phenomenon occurring in numerous engineering applications, physical and natural processes. Due to its importance, a number of studies and textbooks have been published, for example [1-3] among many others, while recent extended reviews are those of [4-7]. One of the first attempts to model droplet evaporation was made by [8] and [9] who proposed the well known 'd^2-law'. This model predicts that the squared diameter of the droplet reduces linearly with time during droplet vaporisation. The model is based on the assumption that the droplet's temperature is uniform and remains constant in time and equal to the wet-bulb temperature. A more realistic approach was proposed by [10] who assumed that droplet's temperature changes in time but not in space by introducing the infinite conductivity model (ICM) and later [11] furthermore assumed that droplet's temperature changes also in the radial direction by proposing the finite conductivity model (FCM). The liquid motion within the droplet was neglected in the previous reported works and was modeled later in [12] by introducing the effective conductivity model (ECM), which combines the FCM with a corrected thermal conductivity that takes into account the internal liquid circulation. The internal liquid velocity field was predefined by assuming that the liquid flow resembles a Hill's vortex. In this work, the effect of the thickening of hydrodynamic and thermal boundary layers, known as Stefan flow, was also implemented by correcting accordingly the heat and mass transfer numbers.

Detailed analysis of the flow field both inside the liquid and the surrounding gas, which was neglected in the previous works, requires the solution of the Navier-Stokes equations. Such an approach was presented in [13, 14] who assumed a spherical droplet shape and used empirical correlations for the Nusselt and Sherwood numbers including the effect of Stefan flow. The same methodology was used in [15] who simulated the experiment of [16] for suspended droplets, but ignoring the presence of the droplet suspender. The presence of the suspender was taken into consideration in a later work of [17]. In this study, the heat conduction from the droplet suspender to the liquid was included under the assumption of a spherical and non-moving droplet. They also proved that a large suspender slows down the liquid motion but promotes the formation of the secondary vortex; they also compared the results obtained for the suspended droplet with the results obtained for a freely moving droplet at the same conditions. Contrary to suspended droplet, in the free moving droplet a secondary vortex was not formed (at least for the Re number examined), while the free moving droplet had a smaller evaporation

rate, mainly due to its deceleration. Generally, it has been acknowledged that the size of the suspender has a relatively small impact on the evaporation rate.

On the other hand, actual fuels blends used with combustion engines consist of many components and thus, their modeling is also of engineering importance. In such systems, the liquid phase properties depend not only on the temperature but also on the species concentration. The latter exhibits gradients inside the droplet's volume resulting from the different evaporation rate of each component. In combination with the liquid circulation, it has been observed that a portion of the most volatile component may be entrapped inside the liquid core towards the droplet centre. Under certain circumstances, this phenomenon can lead to micro-explosion and droplet fragmentation, as discussed for example in [18].

Similarly to the aforementioned modeling studies investigating single-component evaporation, a number of studies examine multi-component evaporation. In the work of [19] the Infinite Diffusivity Model (IDM) and later on in [20], the Finite Diffusivity Model (FDM) have been proposed; most recent works on bi-component droplet evaporation are those of [21, 22].

A detailed modeling of the two-component droplet evaporation was performed by [23] assuming a two-dimensional axially symmetric geometry for a mixture consisting of equal amounts of n-octane and benzene and solving numerically the Navier-Stokes equations. It was observed that there is a preferential evaporation of the more volatile species, while a portion of the later is entrapped inside the recirculation zone developing at the droplet's centre. The work of [24] has demonstrated that for mixtures in which the more volatile component is characterized by higher latent heat of vaporization, it is possible for a poorer in volatile species mixture to evaporate faster than a richer one, due to the higher heating of the droplet. The effect of using variable properties was studied by [25] and it has concluded that the density variation is more essential than the heat capacity variation for the conditions examined.

A moving as well as deformable liquid-gas interface has been also simulated using various methodologies, such as the VOF methodology. Such methods can capture more complicated heat and mass transfer mechanisms compared to those of spherical droplets. The impact and solidification of droplets onto a substrate were modeled in [26-30]. Furthermore, [31, 32] modeled the impact of droplets in hot substrate for a wide range of substrate temperatures and Weber numbers by coupling the VOF methodology with an one-dimensional heat transfer model in the sub-layer between the droplet and the solid wall. Recent work from the author's group has contributed to the calculation of the vapor layer thickness and the droplet levitation from the wall surface, as shown in numerical solution of the Navier-Stokes equations described in [33]. The extension of this work by [34] has focused on the vaporization of a stable droplet in contact

with a heated wall. In [35] the transitional phenomenon prior to droplet deposition was investigated and the cooling effectiveness of the droplet was quantified.

Despite the fact that many of the aforementioned modeling works of [13, 14, 17, 23-25] are quite detailed, their results are not compared with experimental data. Furthermore, the approach of the non-deformable liquid-gas interface limits the generality of these models. On the other hand, predictions employing the VOF methodology may account for the liquid-gas interface deformation. However, such models so far have not been extended in cases which include the evaporation of multi-component liquids.

The present paper represents an extension of the work reported recently by the authors in [36, 37] and examines the evaporation of single- and multi-component droplets under forced convection conditions in a hot air environment using the VOF methodology. Droplets are held in suspension on a spherical extremity and, compared to previous work, the present model accounts for the effect of the deformation of the droplet interface and gives information for the transient motion of the droplet together with a detailed description of the flow field. The numerical model solves simultaneously for the heat and fluid flow both inside and outside the droplet, while it solves simultaneously the evaporation rate of the deformed droplet shape using a local evaporation rate model. At the same time, the species transport conservation equations for the different fuel components are simultaneously solved numerically and account for the preferential diffusion/transport of one species into another, both inside the liquid and the surrounding air phases.

The next section of the paper describes the developed numerical model followed by a description of the test cases simulated. The numerical methodology is similar to that of the recent work of the authors; however, for purposes of clarity and completenes, the full governing equations are presented. The model is first validated against experimental data available in bibliography and then, parametric studies reveal the effect of the most influential parameters.

2   MATHEMATICAL MODEL

In a number of multi-phase flows with well defined interfaces, the liquid to cell volume fraction denoted by α, can be introduced as an additional scalar property identifying the liquid-gas interface; following the approach described in Volume of Fluid (VOF) methodology, as initially proposed by [38], the volume fraction α is defined as:

$$a = \frac{\text{liquid volume}}{\text{total cell volume}} \tag{1}$$

where α takes the value 0 in the gas phase, 1 in the liquid phase and lies between 0 and 1 in the cells containing the interface area. The transport equation of the volume fraction α, including the effects of phase change and liquid thermal expansion is given by:

$$\frac{\partial a}{\partial t} + \nabla \cdot \left(a \vec{u} \right) = -\sum_{k=1}^{ns} \dot{V}_{evap,k}^{vol} - a \frac{1}{\rho_l} \frac{D\rho_l}{Dt} \tag{2}$$

where ns is the number of species by which the droplet is composed and the phase change source term in equation (2) includes the total evaporation of the liquid droplet. The discretisation of equation (2) needs a special treatment in order to avoid numerical diffusion and smearing of the interface. The algorithm described in [39] is used for the discretisation of the convective term, while the Crank-Nicolson time discretisation scheme is employed together with small Courant numbers of the order of 0.2-0.3 for modeling the temporal term. The momentum equations for both phases are written in the form:

$$\frac{\partial (\rho \vec{u})}{\partial t} + \nabla \times (\rho \vec{u} \ \ddot{A} \ \vec{u}) = \nabla \times \vec{T} + \rho \vec{g} + \vec{f}_\sigma \tag{3}$$

where $\vec{u}$ is the velocity vector, $\vec{T}$ is the stress tensor and $\vec{f}_\sigma$ is the volumetric force due to surface tension. Following the approach of [40], the surface tension force is equal to:

$$\vec{f}_\sigma = \sigma \kappa (\nabla a) \tag{4}$$

where σ is the surface tension coefficient, κ is the curvature of the interface while the Marangoni effect has been ignored. The flow field is solved numerically on an unstructured numerical grid using an adaptive local grid refinement technique, as described in detail in [41]. Details for the

discretisation of the above mentioned equations can be found in [42]. Additionally, the transport equations for energy, vapor and liquid species concentration are solved:

$$\rho c_p \frac{DT}{Dt} = \tilde{\nabla} \times (k \tilde{\nabla} T) - \sum_{k=1}^{ns} \dot{m}_{evap,k}^{vol} L_k + \tilde{\nabla} \times \left(\sum_{k=0}^{ns} \rho c_{P,k} T D_{k,m} \tilde{\nabla} Y_k \right) \tag{5}$$

$$(1-a)\rho_g \frac{DY_{g,k}}{Dt} = \tilde{\nabla} \times \left((1-a)\rho_g D_{g,k,m} \tilde{\nabla} Y_{g,k} \right) + \dot{m}_{evap,k}^{vol} \quad , \quad k=1 \div ns \tag{6}$$

$$a\rho_l \frac{DY_{l,k}}{Dt} = \tilde{\nabla} \times \left(a\rho_l D_{l,k,m} \tilde{\nabla} Y_{l,k} \right) - \dot{m}_{evap,k}^{vol} \quad , \quad k=2 \div ns \tag{7}$$

where $D_{g,k,m}$ and $D_{l,k,m}$ are the diffusion coefficients of kth species in the gaseous and liquid mixtures, respectively. Equation (6) is solved for all the vapor species (k=1÷ns), while equation (7) is solved for all liquid species except of the main liquid species (k=1), since its concentration can be computed from the summation of liquid species concentrations, which must equal to one. The solution of the extra equation (7) and its coupling with equations (5) and (6) represents an innovative point of the present work.

Cell properties are calculated according to [42] e.g.:

$$\begin{aligned}
\rho &= a\rho_l + (1-a)\rho_g \\
\mu &= a\mu_l + (1-a)\mu_g \\
c_p &= \frac{a\rho_l}{\rho} c_{p,l} + \frac{(1-a)\rho_g}{\rho} c_{p,g} \\
k &= ak_l + (1-a)k_g
\end{aligned} \tag{8}$$

Gas phase properties are mass averaged with the vapor concentration, taking into consideration all the species existing in the gaseous phase:

$$\varphi_g = \sum_{k=1}^{ns} Y_{g,k} \varphi_{vap,k} + (1 - \sum_{k=1}^{ns} Y_{g,k}) \varphi_{air} \quad ,$$

$$\rho_g = \frac{p \cdot MW}{\bar{R}T} \quad , \quad MW = \left(\sum_{k=1}^{ns} \frac{Y_{g,k}}{MW_{vap,k}} + \frac{1 - \sum_{k=1}^{ns} Y_{g,k}}{MW_{air}} \right)^{-1} \tag{9}$$

where $\varphi = \mu, k, c_p$

Liquid phase properties are also mass averaged with liquid concentration:

$$\rho_l = \left(\sum_{k=1}^{ns} \frac{Y_{l,k}}{\rho_{l,k}} \right)^{-1} \quad , \quad \varphi_l = \sum_{k=1}^{ns} Y_{l,k} \varphi_{l,k} \tag{10}$$

where $\varphi = \mu, k, c_p$, and subscript 1 refers to the main liquid component, which is n-decane in the present work. The properties of the pure components are assumed to be function of temperature according to [43] and are updated at every iteration during the numerical solution. It has to be noted that for the estimation of the mixture properties, more accurate but also more complex expressions like those reported in [44] could be used. Despite the fact that equations (9) and (10) represent crude approximations of the estimation of mixture properties, they provide sufficient accuracy without complicating further the already complex model developed.

The evaporation rate model employed is stemming from Fick's law and uses the vapor concentration gradient at the liquid-gas interface as the driving force inducing vaporization; it further assumes that the interface is saturated. The evaporation rate, which is independent of flow conditions and interface shape, is given by:

$$\dot{m}_{evap,k} = \frac{dm_k}{dt} = \rho_g D_{g,k,m} A_{l,cell} \left(\frac{dY_{g,k}}{dn} \right)_{surf} \quad , \quad A_{l,cell} = V_{cell} \left| \tilde{\nabla}a \right| \quad , k=1 \div ns \tag{11}$$

Although the evaporation rate is proportional to the concentration gradient, the vapor advection is taken into account though the solution of the Navier-Stokes equations; the predicted flow field convects away the vapor produced and thus, modifies the local vapor concentration gradient values around the droplet. The saturated vapor concentration is given by the Clausius-Clapeyron equation; it can be found for example in [2] among others.

The main difference of the evaporation rate used in the present study relative to the aforementioned studies discussed in the introduction section of the present article, is the way that the evaporation rate is applied at each computational cells. In past works, the interface was assumed to be infinitely thin and the evaporation rate was applied as a boundary condition on the interface region. Here, the interface region is part of the solution domain and the evaporation rate is distributed in the computational cells lying in the interface region, by calculating the surface area $A_{l,cell}$ of the liquid in the computational cell. On the other hand, zero- and one-dimensional models are not applicable in the framework of the VOF methodology. This is because such models assume some field reference conditions, such as free stream temperature and velocity, as well as a reference geometrical scale, such as droplet diameter. It is also of importance to notice that the present model does predict the shape deformation, the motion and the final position of the droplet suspended on a thin suspender under the combined influence of gravity and opposite direction drag force resulting from the convective flow field; more details will be shown in section 4.2.

The numerical results to be presented here have been obtained using the GFS code [45], which has been validated against experimental data and used in the recent studies of [33-37, 42, 46-49].

The integral magnitudes φ in liquid phase presented here are calculated using a volume average formula:

$$\varphi_{mean} = \frac{\sum\limits_{cells} \varphi_{cell} \, a_{cell} V_{cell}}{\sum\limits_{cells} a_{cell} V_{cell}} \tag{12}$$

The equivalent droplet diameter (since the droplet deforms) is calculated from the instantaneous liquid volume, i.e.:

$$d = \left(\frac{6 \sum\limits_{cells} a_{cell} V_{cell}}{\pi} \right)^{\frac{1}{3}} \tag{13}$$

Time is non-dimensionalised using an estimation of the total evaporation time inspired by the d^2-law as:

$$\tau = \frac{t}{t_{C10}} \qquad (14)$$

This time scale t_{C10} corresponds to the total evaporation time of the pure n-decane droplet, which is the less volatile species examined here. For reasons of uniformity, it is used for all mixtures examined, including also for the less volatile pure n-heptane droplet. This time scale can be calculated as:

$$t_{C10} = \frac{d_0^2}{\zeta_{C10}} \text{ , where } \zeta_{C10} = \frac{4 Sh_0 \rho_{g,\infty} D_{g,C10}}{\rho_{l,C10}} \ln\left(1 + B_{M,C10}\right) \qquad (15)$$

The initial Sherwood number Sh_0 is calculated from the Ranz-Marshall correlation [50]. It is based on the initial droplet diameter while all properties are calculated at the gas phase infinity conditions except for the n-decane's diffusion coefficient $D_{g,C10}$ and the Spalding number $B_{M,C10}$, which are calculated at the wet bulb temperature of n-decane. Finally, the Reynolds number is calculated using the gas phase properties far from the droplet, in contrast to [36] in which film conditions were assumed. This was found more convenient for the calculation of the initial Sherwood number, as also for the calculation of the factor FR_0 which is indicative of the equilibrium position of the droplet, as it will discussed in more detail in section 4.2.

3   DESCRIPTION OF TEST CASES SIMULATED

The mathematical model used is initially validated against the experimental data of [51] who examined the evaporation of suspended droplets subjected successively to natural and forced convection flow conditions. Six of the experiments described in [51] have been simulated and examine the evaporation under forced convective conditions of a pure n-heptane droplet (case e1), a pure n-decane droplet (case e6) and mixtures of the two species at various composition by volume of n-heptane (cases e2-e5); the details are shown in Table 1. The notation «e» in case naming denotes that these cases refer to experimental data, and thus, they can be distinguished from those referring to the following parametric studies.

Details for the experimental set-up simulated here and used for model validation can be found in the relevant article [51]. In brief, the droplets were placed in a wind tunnel and were held in suspension at the spherical head (400μm) of a capillary tube (200μm), which was placed

perpendicularly to the gas flow, under atmospheric pressure. The droplet diameter was recorded with a video camera which was synchronized with an infrared thermo-graphic system for obtaining droplet's surface temperature measurements. Since the droplet takes a deformed shape during its vaporization process, the reported results refer to that of an equivalent droplet diameter having the same volume as that of the deformed one. A three-dimensional representation of one of the cases simulated is shown in Fig. 1, where the numerical grid with the local refinement around the gas liquid interface is shown, together with details of the flow development both inside the liquid phase and the surrounding gas.

In Fig. 2a, the computational domain at the beginning of the simulation and the boundary conditions are shown together with the details of the numerical grid shown in Fig. 2b; at the vicinity of the gas-liquid interface, one-, two- and three-levels of local grid refinement have been tested. The flow has been considered to be two-dimensional and axi-symmetric. This can be justified from the works of [52, 53] amongst others, since the maximum Re number is around 220 for all cases examined and decreases as the droplet diameter decreases during its vaporization process. At the inlet of the computational domain dry air, constant velocity, constant temperature and zero 1st gradient for the pressure have been assumed. At the outlet of the computational domain the pressure is set equal to the atmospheric one, while zero 1st gradient boundary condition have been assumed for all other flow variables. Western and eastern boundaries are assumed to be a free stream and a symmetry axis respectively, which correspond to a zero 1st gradient boundary condition for all variables except for the velocity normal to the boundary, which is set equal to zero. Finally, the spherical head of the suspender is assumed to be an adiabatic and impermeable wall. As far as initial conditions are concerned, a uniform temperature and liquid concentration fields have been assumed, while the spherical head has been placed symmetrically at the center of the droplet. Finally, it could be mentioned that the initial liquid volume is less than 2% of the volume of the computational grid.

In order to check if grid independence of the results has been achieved, the reference case, which is described in detail in section 4.3, has been simulated using 1, 2 and 3 levels of local grid refinement. Details of the corresponding grid at the region of the gas-liquid interface are shown in Fig. 2b. The results for the non-dimensional droplet volume variation with time are presented in Fig. 3; as it can be seen in this figure, grid independence can be achieved using 2-levels of local grid refinement. On the other hand, use of 3-levels of local grid refinement results to increased computational cost. So, using 2-levels of local grid refinement has been considered as a good compromise between accuracy and computational time. The spherical support of the droplet is modeled with an unstructured base grid. This resulted in a numerical grid of

approximately 4500 cells at the beginning of the simulation; the cell size at the interface region is approximately 2.6% of the droplet radius; simulations using a uniform grid having the resolution of the interface would require approximately 315,000 cells. Depending on each case, the simulations can last approximately 1-3 CPU months; this is mainly due to the time step limitation of the VOF methodology, which requires small Courant number of the order of 0.2-0.3 in order to avoid numerical diffusion.

4   RESULTS & DISCUSSION

4.1   Model validation

In this section the numerical model using the VOF methodology is validated against the experimental data reported in [51] for the cases described above; the relevant conditions are summarized in Table 1. The temporal evolution of the non-dimensionalised droplet squared diameter for all cases examined is presented in Fig. 4a,b, while in Fig. 4c,d,e the temporal evolution of mean droplet temperature is presented for the cases in which experimental data were available. Furthermore, along with the present predictions, the predictions reported by [51, 54, 55], who used one-dimensional models are presented together with the predictions of [56]; the latter have used a two-dimensional model to account for the Hill's vortex. Predictions for the droplet size are in good agreement with the experimental data for the rich in n-heptane droplets; some deviations can be observed at the latter stages of the process in which the less volatile n-decane dominates the phenomenon. The same trend is also observed for the predicted droplet temperature. The prediction for the wet bulb temperature of the droplet at the later stages of evaporation is overestimated approximately by $6^{o}C$. On the other hand, this overestimation has been also observed in most of the previous studies and may be attributed to the physical properties library values used, as numerous studies non reported here have indicated. The physical processes taking place during multi-component droplet evaporation will be discussed in detail in sections 4.3 and 4.4, while the influence of specific parameters in section 4.5. An extended investigation of the physical processes and the flow field regimes for the case e2, can be found in [36].

4.2 Droplet equilibrium position and droplet deformation

Before proceeding to the detailed transport phenomena description, it is important to mention that the VOF methodology employed here predicts that the droplet is moving on the suspender as a result of gravity and aerodynamic forces while it is simultaneously being held by the suspender due to the adhesion forces. Since there were no available experimental pictures, the wettability of the liquid with the solid suspender was taken into consideration by setting a typical contact angle of n-decane in touch with glass, since the volatile n-heptane vaporizes faster, leaving the n-decane behind towards the later stages of the process. The advancing and receding contact angle values used are 90 and 10 degrees, respectively. Initially, the spherical suspender lies at the centre of the droplet, as shown on Fig. 5a. In the work of [17] the droplet was assumed to be motionless despite the action of two forces acting initially on the droplet, namely the droplet's weight (B) and drag force due to air flow (F_D). In the present study, an extension of this work is considered by allowing the droplet to move according to the forces acting on it. The ratio of the magnitude of these two forces, denoted here as FR, provides at every time step an indication for the droplet movement direction. Depending on FR, the droplet can move in the direction of gravity or the opposite one. The value of FR can be calculated using the drag coefficient as in [12] as:

$$FR = \frac{B}{F_D} = \frac{mg}{c_D \frac{1}{2}\rho_{g,\infty}u_\infty^2 \frac{\pi}{4}d^2} = \frac{4\rho_l dg}{3\rho_{g,\infty}u_\infty^2 c_D} \quad , \quad c_D = \frac{24}{Re}\left(1 + \frac{1}{6}Re^{2/3}\right) \tag{16}$$

For the pure n-heptane droplet (case e1) the ratio of the forces acting initially on the droplet is $FR_0 \approx 1.0$, indicating that initially the droplet's weight is almost equal to the drag force. As the droplet starts to evaporate, it becomes lighter and thus, it is moving in the direction of the flow, as shown in Fig. 5b, until it reaches within a short period of time the equilibrium position shown on Fig. 5c. Adhesion forces, resulting from the loss of symmetry of the droplet shape relative to the suspender, oppose droplet detachment from the surface; the droplet remains attached to the suspender for the rest of the evaporation process (Fig. 5d-f) while its center of mass recedes towards the spherical head.

For the case of the larger mixture droplet (case e2), the initial force ratio is $FR_0 = 1.50$, thus the droplet's weight is now greater than the aerodynamic drag force. As a result, the droplet moves in the direction of gravity, which is shown in Fig. 6b, until it reaches again the equilibrium position of Fig. 6c. As further vaporization results to loss of liquid mass, the suspended droplet becomes gradually lighter and at the time instant of Fig. 6d, the drag force becomes again greater than the droplet's weight, similarly to the previously described case. From this time

onwards, the droplet moves to the direction of the flow, as shown in Fig. 6e and Fig. 6f, until its complete vaporization. It is interesting to notice that, in this case, a small meniscus is formed at the upper part of the suspender, as shown in Fig. 6d. The formation process of this meniscus can be explained with the aid of Fig. 6g, which shows the dimensionless pressure, defined as $p^* = (p - p_\infty)/(\frac{1}{2}\rho_{g,\infty}u_\infty^2)$, together with the flow streamlines just before the creation of the meniscus. In the downstream part of the droplet, increased pressures can be observed together with the formation of two relatively small-scale recirculation zones with opposite rotational motion. These two opposite rotating fluid zones and the presence of the suspender lead to the formation of a liquid neck on the solid surface; finally, the liquid present to the right-hand-side of the neck pinches off, creating a meniscus at the rear part of the suspender.

The temporal motion of the center of liquid volume for all cases examined is presented in Fig. 7a. As it can be seen, the droplets of cases e1, e3 and e4 for which FR_0 is less than unity, are moving in the direction of the flow while for the rest of the cases the droplet moves in the direction of gravity. The abrupt movement of the droplet corresponding to case e2 is also shown, while the wavy form of curves reveal the small oscillatory motion of droplets. On the other hand, as already mentioned, droplets deform as it can be seen for example Fig. 6c. A measure of their deformation can be estimated by comparing the instantaneous droplet surface area with that of a sphere having with the same volume. Thus, the factor sph, which is always greater than one, is used:

$$sph = \frac{A_{liq}(t)}{A_{sphere}(t)} = \frac{\sum_{cells}\left(|\nabla a|V_{cell}\right)}{\pi d^2} \qquad (17)$$

where, the droplet diameter is calculated from equation (13). This magnitude is plotted in Fig. 7b. Its wavy form is a result of the small oscillations that the droplets perform; as it can be seen, the deformation from the idealized assumption of a spherical droplet is relatively small, justifying the assumptions of previous studies for spherical droplets. It has also to be noted that at time t=0 at which the spherical extremity lies at the centre of the droplet, the factor sph has a non-unity value; this value depends on the relative size of the droplet radius and suspender's radius.

4.3   Description of multi component droplet evaporation

In this section a detailed analysis of the multi component droplet evaporation will be presented. A typical case, denoted hereafter as reference case is examined; the details of this case are summarized in Table 2.

In Fig. 8a the temporal evolution of the droplet's squared diameter and droplet's mean temperature in dimensionless form are presented together with the instantaneous concentration of n-heptane. In Fig. 8b the temporal evolution of the droplet's total evaporation rate, normalized with the initial droplet mass, along with the evaporation rate of each species independently is shown; for a straight comparison with Fig. 8a, the instantaneous concentration of n-heptane is also plotted.

The evaporation process can be divided in two stages; each of them is characterized by the preferential evaporation rate of the two liquid species comprising the initial mixture. The evaporation of the more volatile n-heptane component dominates the process at the first stage of the process; when most of the volatile component has been evaporated, the phenomenon is controlled by the evaporation of the less volatile species. At the first stage, when n-heptane's concentration is higher than 0.3 and $\tau<0.2$, the multi component droplet behaves as a single component droplet; the regression of the droplet surface area seems to obey the d^2-law and droplet's temperature increases, tending to reach the wet bulb temperature of n-heptane at the corresponding flow conditions. Later on, due to the reduction of the concentration of the more volatile component, the less volatile n-decane starts to evaporate and when $Y_{C7,mean}\approx0.2$, a change in the slope of squared diameter curve can be observed; following this moment, the contribution of the less volatile n-decane to the evaporation process starts to be equally important until it dominates the whole process. The droplet is further heated until the more volatile component has been completely vaporized ($\tau=0.3$) and the droplet finally reaches the wet bulb temperature, which is that of the pure n-decane at the given flow conditions. The wet bulb temperature is reached when the convention heat flux from the surrounding gas becomes equal to the heat flux required for evaporation. The wet bulb temperature is always lower than the gas phase temperature and for the conditions shown in Table 2, the droplet's dimensionless temperature reaches a value of 0.8. This distillation-type behavior for low evaporation rate conditions, has been also reported in [57].

4.4 Flow field regimes

In this section the flow field distribution and the underlying transport processes are discussed in more detail. The following figures refer to the reference case of Table 2 and since $FR_0<1$, the droplet moves opposite to the direction of gravity. On the left-hand-side of Fig. 9 the spatial distribution of the velocity magnitude, non-dimensionalised with the free stream velocity, can be seen. On the right-hand-side the streamlines both for the liquid and gaseous phases are shown; at the lower part of Fig. 9 the details of the flow field are also presented. A large

recirculation zone is formed inside the liquid mass; downstream of the droplet and inside the wake region a recirculation zone with the same direction of rotation as that inside the liquid is also formed. The aforementioned recirculation zones play an important role in the physical processes taking place during droplet evaporation and it will be further discussed later.

Increased normalized velocities of the order of 1.1 are observed over the droplet while the recirculation inside the gas extends initially to a region of approximately 0.8d with a dimensionless velocity magnitude less than 0.15 and becomes shorter with time, as the Re number decreases. It has also to be noted that at the rear of the droplet, inside its wake, there is an almost stationary zone as highlighted by the zoomed regions of Fig. 9. This is attached to the droplet together with the formation of small cellular zones. The thickness of this zone is approximately $0.04d_0$ and remains almost constant in time. In this region there is high vapor concentration values and low velocity values.

Compared to the length of the recirculation region formed behind a solid sphere under steady-state flow conditions, the predicted recirculation flow length of the evaporating droplet is much smaller for the same Reynolds number. Thus is mainly due the vortex motion of the liquid mass inside the droplet, which retards flow separation towards the rear of the droplet and suppresses the length of the wake, as also reported previously in [2]. The dependence of the recirculation length on Re number is shown in Fig. 10c for some of the cases examined; the experimental data of [58] for a solid sphere are also shown. The Re number used is based on the relative liquid-gas velocity according to the estimation of maximum liquid surface velocity presented in [12]. This assumption takes into consideration both the ratio of liquid to gas viscosities and the evaporation rate of the droplet. A satisfactory approximation of the wake length is also shown in Fig. 10c. In Fig. 10a and Fig. 10b, the flow field for two cases with different Re numbers is shown; for Re values smaller than 30, no recirculation zone in the gaseous phase has been observed. The velocities inside the liquid phase are much smaller than the velocities in the gaseous phase; their magnitude doesn't exceed 6% of free stream velocity which is in agreement with the works of [59, 60]. In these works, a vortex model was developed and it was proved that the velocities inside the liquid are less than one order of magnitude compared to the free stream velocity. Inside the liquid two recirculation zones are formed; the bigger one occupies most of the droplet volume while the smaller one is formed at the rear of the droplet and it is clearly shown in the magnified regions of Fig. 9. According to [2], the second recirculation is often observed, but it is too small and can be ignored. Thus, the flow inside the droplet can be approximated as a Hill's vortex; this comment is justified for the initial stages of the droplet evaporation. The simulations performed here reveal that the length of the second vortex along the x-axis, is approximately $0.04\text{-}0.06d_0$ and remains almost constant with time; this length is very small at the initial stages of the process when compared to the initial droplet diameter, but

it becomes progressively larger and larger; at τ=0.55 its length is ∼0.11d. The same trend for the second vortex was also observed in [17]. The centre of the big vortex in the x-axis does not coincide with the corresponding centre of liquid volume, mainly due to the presence of the solid suspender and the formation of the secondary vortex. Theoretically, based on the Hill's vortex model (see [2] among others), the vortex centre should be located at 90° from the front stagnation point and at a distance of $R/\sqrt{2}$ from the axis of symmetry. The present simulations reveal that the centre of the big vortex moves during evaporation from 87° to 101°, while its distance from the axis of symmetry varies from 0.73-0.83R; these values are slightly higher from the theoretical ones that ignore the presence of the suspender.

The distribution of the dimensionless x-component velocity component u_x/u_∞ and the dimensionless vorticity are shown in Fig. 11a; these profiles have been extracted on the radial direction passing through the centre of the main liquid vortex while the plotted curves correspond to five time instances. Similarly, the distribution of the dimensionless stream-function $\psi/(u_\infty R^2)$ along the same location and times is shown in Fig. 11b; the vorticity and the stream-function are non-dimensionalised with the instantaneous equivalent droplet radius. The absolute values of the dimensionless velocity and stream-function become smaller as time progresses due to Re number regression. This is in accordance with the findings of [14] and [17], while the stream-function reaches its maximum at the centre of the vortex. On the other hand, the dimensionless vorticity varies almost linearly in the radial direction; the slightly distorted values near the liquid-gas interface are only numerical artifacts arising from VOF-based discretisation of the liquid-gas interface.

In Fig. 12 the predicted gas phase non-dimensional isotherms are shown at various time instants for the reference case. A relatively thick thermal boundary layer develops upstream of the droplet. Its thickness around the middle part of the droplet doesn't change significantly with time. The spatial distribution of the isotherms downstream the droplet follows the flow field in the wake formed in the gaseous phase; the temperature wake shrinks as time progresses. It is also of interest to notice that maximum evaporation occurs from the front part of the droplet. At the same time, the location of the droplet on the suspender remains almost constant until full vaporisation. This indicates that the internal fluid circulation transfers continuously liquid from the rear part of the droplet to the front, balancing the loss of mass due to evaporation.

Results for the vapor concentration field for the reference case are shown in Fig. 13. In this plot, the vapor concentration field is expressed as the ratio of the vapor pressure of each component normalized with the corresponding saturation vapor pressure of the same component at the same

cell temperature. This normalization provides a better insight of the physical phenomenon, since the actual mass fraction of each component in the gaseous phase exhibits very different values due to pure species volatility difference. In Fig. 13, the left-hand-side corresponds to n-decane's normalized vapor pressure and the right-hand-side represents the same magnitude but for the n-heptane component. Values of this relative saturation ratio cannot exceed the corresponding values of liquid molecular fraction of each component. At the initial stages of the process, e.g. $\tau=0.048$ when the more volatile n-heptane is vaporizing faster, the normalized vapor pressure exhibits large values at the gas-liquid interface region. The opposite behavior is observed for the less volatile n-decane component. Similarly to the thermal boundary layer and velocity wake of the gas flow, the concentration boundary layer and its wake have a similar topology; strong concentration gradients develop at the front part of the droplet while further downstream the spatial distribution is affected by the presence of the recirculation zone. It is also worthwhile to refer that the spatial distribution of the concentration fields for both species exhibit similarities but with a time delay.

In Fig. 14 the temperature field and the n-heptane concentration fields inside the liquid droplet are presented for the reference case on the left- and right-hand-sides, respectively, at two time instances. Due to low evaporation rate, the thermal and concentration gradients that develop inside the liquid mass are quite weak; so it has been considered more convenient to plot the difference of their magnitude from the corresponding mean value at the same time together with the corresponding mean mass averaged value for the temperature and the n-heptane concentration. As it can be seen, the relatively low evaporation rate in combination with the homogenization of the liquid composition caused by the internal liquid circulation [61], results to almost negligible differences from the mean values. Furthermore, small temperature and concentration differences imply that neglecting the Marangoni effect on surface tension is a reasonable hypothesis, while infinite conductivity and infinite diffusivity models could be used for fast predictions. Despite the fact that the temperature and concentration gradients inside the droplet are small, the numerical finding of [23] is verified by the present predictions; inside the liquid core slightly increased values of the concentration of the volatile n-heptane are observed throughout the evaporation process. This results from the combination of the internal liquid circulation and the diffusion process of n-heptane inside the liquid. At later times, lack of the more volatile specie is observed in the rear part of the droplet.

4.5   Parametric investigation of droplet evaporation

Following model validation, a set of parametric studies are performed in order to reveal in detail the influence of various parameters on the complicated thermo-fluid dynamics and phase-change processes taking place during the multi-component evaporation process. The parameters investigated include the effect of initial concentration, droplet diameter, gas temperature and species volatility difference. The reference case of Table 2 is common for all the tests performed while only one parameter is changing in each numerical test. Such studies have also been presented before in the literature using zero-, one- and two-dimensional models but is was considered of interest to verify past finding using the complete differential flow, heat transfer and phase-change equations employed here.

Initially, the effect volatile n-heptane concentration in the mixture is examined. Then, droplets consisting of 75% by mass of n-heptane and variable heavier components are considered and the effect of droplet size and gas phase temperature is investigated. The cases examined are summarized in Table 3; on this table, blank cells denote values equal to those of the reference case which are shown on the top row of the table.

4.5.1   Influence of droplet mixture composition

Droplets with 1mm diameter and 300K initial temperature are exposed in a convective environment of 350K temperature, under atmospheric pressure and 3.2m/s free stream velocity. Five initial mass concentrations of n-heptane in liquid are studied: 100% (pure heptane), 75% (reference case), 50%, 25% and 0% (pure decane). The time is non-dimensionlized with the time-scale corresponding to the lifetime of pure decane, which is t_{C10}=21.041s for the given conditions.

Fig. 15 shows the temporal evolution of the droplet's squared diameter and its mean dimensionless temperature. The evaporation of the pure species droplet obeys the d^2-law, while the size regression of the pure n-decane droplet slightly deviates from the d^2-law at the initial stages of the evaporation process due to initial droplet heat-up. The mean volume-averaged temperature of the pure species droplet is continuously increasing but at a decreasing rate, until it reaches the wet bulb temperature and remaining constant hereafter.

The transitional behavior described in section 4.3 is also observed here and becomes more intense with the increase of the initial concentration of the volatile component. This is evident from the marked change of the slope of the curve describing the size regression of the 75%

mixture compared to the corresponding of the 25% mixture. This is in agreement with the temperature curves, where the rich volatile-component mixture exhibits a nearly isothermal period ($\tau \approx 0.1$); contrary to that, this behavior tends to vanish when the initial concentration of the volatile component is decreasing.

The evaporation rate of the droplet is shown in Fig. 16a; as it can be seen, it increases with increasing concentration of the volatile n-heptane component in the mixture. Its temporal variations exhibits a peak followed by a continuous decrease. This behavior is due to the fact that the evaporation rate increases with droplet temperature and droplet size. During the evolution of the phenomenon, droplet's temperature increases but droplet's diameter decreases. Furthermore, the evaporation of mixture droplets exhibits a distillation-type behavior as already described in section 4.3. This is valid for all mixtures irrespectively of the initial concentration of the volatile component. The later can be justified by examining Fig. 16b in which the contribution of the volatile n-heptane in the total evaporation rate is presented. At the initial stages of the evaporation process and irrespectively of the initial concentration of the volatile n-heptane component, the total evaporation rate is defined mainly by the evaporation of the more volatile component.

Another interesting point that deserves to be addressed is that the final wet bulb temperature for all droplets containing n-decane is the same, irrespectively of the initial concentration of n-heptane. This was expected since at the later stages of evaporation when the wet bulb temperature is reached, only the less volatile n-decane remains and the droplet behaves as if it was a single-component droplet. Numerically, this is achieved by taking into consideration the species diffusion term for multi-component mixtures appearing to the right-hand-side of the energy equation (5):

$$\tilde{\nabla} \times \left(\sum_{k} \rho c_{P,k} T D_{k,m} \tilde{\nabla} Y_k \right) \qquad (18)$$

This term, must be included in the energy equation even if a single component droplet is simulated, since the surrounding gas is a mixture of air and vapor. The influence of ignoring this term in single component droplets can be found in [37] and leads to different wet bulb temperatures for pure species and mixtures for the same flow conditions.

4.5.2 Influence of droplet diameter, gas temperature and species volatility

In this section, multi component droplets containing 75% by mass n-heptane are examined in order to reveal the effect of droplet size, gas phase temperature and species volatility difference. Three droplet diameters are studied: 0.1mm, 0.2mm and 1.0mm (reference case), while it is important to notice that the ratio of the initial droplet diameter to the suspender diameter, remains unchanged. Similarly, three surrounding air temperatures are considered: 350K (reference case), 400K and 450K. It is of importance to emphasize here that even for the higher temperature value, equilibrium thermodynamic conditions apply. Finally, binary droplets consisting of n-decane and four different chemical species are tested. The dissolved in n-decane species are n-hexane, n-heptane (reference case), n-octane and n-nonane. In the following Fig. 17 the temporal evolution of non-dimensional droplet's squared diameter and dimensionless droplet temperature is shown, while the time axis is normalized with n-decane droplet lifetime.

From Fig. 17 it is concluded that in dimensionless form, the evaporation of multi component droplets exhibits the same behavior for all cases examined. The d^2-law for each component separately is confirmed for all cases, while the wet bulb temperature is mainly controlled by the gas phase temperature. Droplet size doesn't affect the transitional behavior of droplet evaporation, despite the fact that the total evaporation time of a droplet is proportional to d_0^2. The transitional behavior tends to disappear with increasing gas phase temperature and decreasing species volatility difference, which is in agreement with the findings of [57]. Increase of the gas phase temperature results to decreased actual droplet lifetime and increased wet bulb temperature in dimensional units. On the other hand, in non-dimensional units, the opposite behavior is observed; dimensionless wet bulb temperature decreases with increasing gas phase temperature.

For the cases with variable species volatility difference, the mixture containing n-hexane experiences an intense transitional behavior. On the other hand, the n-nonane mixture exhibits a very weak transitional behavior. The droplet's temperature reaches the same wet bulb temperature for all mixtures, since the less volatile n-decane controls the second stage of evaporation. It is interesting to observe that the temperature of the n-hexane's mixture, initially decreases and then increases; this is due to the wet bulb temperature of the pure n-hexane, which is lower than the initial temperature of the droplet.

Finally, it has to be noted that the case with 450K gas phase temperature is characterized by a high evaporation rate; the later in combination with the accumulation of numerical errors resulting from the large number of computational time steps, resulted in smearing and diffusion

20

of the gas-liquid interface. So the simulation was stopped earlier compared to other runs, since from this point and afterwards, predictions were not considered reliable. This problem was partly suppressed by using even smaller Courant number and a liquid-gas interface sharpening technique, which reduced the numerical diffusion at the interface.

5   CONCLUSIONS

A Navier-Stokes equation numerical methodology coupled with an evaporation model and the VOF methodology, utilizing an unstructured dynamically adapting computational grid, have been used to numerically predict the evaporation process of a droplet consisting of one or two components at various concentrations. The droplet was suspended in the spherical extremity of a capillary tube under convective flow conditions. The model used has been initially validated against experimental data, referring to both single- and binary mixture droplets, showing good agreement.

The VOF methodology proved to be capable of predicting droplet motion, droplet shape and droplet final position on the solid suspender as also accurate evaporation rates both for single and binary mixtures. The components of the binary droplet are preferentially evaporated and a distillation-type evaporation process takes place. A d^2-law type of evaporation is observed in two stages. Initially the droplet tends to reach a wet bulb temperature since evaporation is dominated by the more volatile species; then a heat-up follows and when the more volatile n-heptane has been nearly fully vaporized, droplet's temperature reaches the wet bulb temperature of pure n-decane. This transitional behavior is independent of the droplet size and tends to be more intense for rich in volatile mixtures, as also in cases with a low evaporation rate and large volatility differences between mixture species.

A detailed description of the flow variables both in the gaseous and the liquid phases has been presented. The recirculation zones formed inside the liquid and gas phases play an important role on the spatial distribution of flow variables. In the gas phase, the recirculation zone is much smaller compared to the one corresponding to a solid sphere with the same Reynolds number. Its length reduces with time due to droplet evaporation and thus to Re number reduction. Inside the liquid two recirculation zones are formed comprising a main vortex and a smaller one; the latter occupies an almost constant with time length at the rear part of the droplet, thus increasing its relative size compared to the decreasing droplet diameter. The vorticity of the main vortex reduces from the droplet symmetry axis to the droplet surface but remains almost constant with

time. The presence of the solid suspender along with the oscillations of the droplet moves the centre of the big vortex further off the symmetry axis and towards the rear stagnation point. Finally, a vapor layer consisting of organized vapor cells seems to be formed around the evaporating droplet having a size of $0.04d_0$.

Strong thermal and concentration gradients are formed at the front of the droplet, while downstream the corresponding spatial distribution is affected from the recirculation inside the gas phase. Inside the droplet, the temperature and concentration fields proved to be almost uniform due to the low evaporation rate of the cases examined. This justifies the use of infinite conductivity and infinite diffusivity models (ICM and IDM) for predicting droplet evaporation.

6   NOMENCLATURE

Symbol	Quantity	SI Unit
A	Surface area	m^2
B	Weight	N
c_D	Drag coefficient	-
c_p	Heat capacity	$J/(kg \cdot K)$
d	Diameter	m
D	Diffusion coefficient	m^2/s
F_D	Drag force	N
$\overset{\text{\tiny{1}}}{f}_\sigma$	Surface tension force	N
g	Gravity acceleration	m/s^2
k	Thermal conductivity coefficient	$W/(m \cdot K)$
L	Latent heat of vaporization	J/kg

l	Length	m
m	Mass	kg
MW	Molar weight	kg/kmol
n	Normal coordinate to gas-liquid interface	-
ns	Total number of liquid species	-
p	Pressure	N/m^2
$\bar{R}$	Universal gas constant (=8314)	$J/(kmol \cdot K)$
R	Radius	m
r	Coordinate in radial direction	m
sph	Deviation from spherical shape	-
T	Temperature	K
T^*	Dimensionless temperature $\left(T - T_{d0}\right)/\left(T_\infty - T_{d0}\right)$	-
$\overset{\scriptscriptstyle 1}{T}$	Stress tensor	N/m^2
t	Time	s
t_{C10}	n-decane droplet lifetime	s
u	Velocity	m/s
V	Volume	m^3
x	Coordinate in direction of flow	m
Y	Mass concentration (kg/kg)	-
Y_{vol}	Volume concentration (m^3/m^3)	-

Greek Symbols

Symbol	Quantity	SI Unit

23

α	Liquid volume fraction	-
ζ	Evaporation constant	m²/s
κ	Curvature	m⁻¹
μ	Viscocity	kg/(m·s)
ρ	Density	kg/m³
σ	Surface tension coefficient	N/m
τ	Non-dimensional time $\tau = t / t_{C10}$	-
φ	General symbol for fluid physical property	
ψ	Stream function ($u = -\dfrac{1}{r}\dfrac{\partial \psi}{\partial r}$)	m³/s
ω	Vorticity	s⁻¹

Subscripts

Symbol	Quantity
cell	Cell
d	Droplet
evap	Evaporation
exp	Experimental
g	Gas phase
k	k^{th} species of the mixture
l	Liquid phase
m	Mixture
mean	Mean
0	Initial

rel	Relative
s	Saturated
surf	Surface interface
vap	Vapor
∞	Conditions at the inlet of the computational domain

Superscripts

Symbol	Quantity
$\dot{\varphi}$	Time rate of φ
φ^{*}	Dimensionless φ
φ^{vol}	φ volumetric [units φ]/m^3

Non-dimensional numbers

Symbol

B_M	Spalding number $B_M = \dfrac{Y_{g,s} - Y_{g,\infty}}{1 - Y_{g,s}}$
Re	Reynolds number $Re = \dfrac{\rho_{g,\infty} d_0 u_{\infty}}{\mu_{g,\infty}}$
Sh	Sherwood number $Sh = 2 + 0.6\,Re^{1/2}\,Pr^{1/3}$

abbreviations

C10	n-decane
C7	n-heptane

C8	n-octane
C9	n-nonane
ECM	Effective Conductivity Model
FCM	Finite Conductivity Model
FDM	Finite Diffusivity Model
FR	Force ratio
ICM	Infinite Conductivity Model
IDM	Infinite Diffusivity Model
VOF	Volume Of Fluid

7   REFERENCES

[1] R. Clift, J.R. Grace, M.E. Weber, Bubbles, drops and particles, Academic Press, New York, 1978.

[2] W.A. Sirignano, Fluid Dynamics and Transport of Droplets and Sprays, Cambridge University Press, 1999.

[3] R.B. Bird, W.E. Stewart, E.N. Lightfoot, Transport Phenomena, 2nd ed., Wiley, New York, 2002.

[4] S.D. Givler, J. Abraham, Supercritical droplet vaporization and combustion studies, Progress in Energy and Combustion Science, 22 (1996) 1-28.

[5] R.S. Miller, K. Harstad, J. Bellan, Evaluation of equilibrium and non-equilibrium evaporation models for many-droplet gas-liquid flow simulations, International Journal of Multiphase Flow, 24 (1998) 1025-1055.

[6] J. Bellan, Supercritical (and subcritical) fluid behavior and modeling: drops, streams, shear and mixing layers, jets and sprays, Progress in Energy and Combustion Science, 26 (2000) 329-366.

[7] S.S. Sazhin, Advanced models of fuel droplet heating and evaporation, Progress in Energy and Combustion Science, 32 (2006) 162-214.

[8] G.A.E. Godsave, Burning of Fuel Droplets in: 4th International Symposium on combustion, The Combustion Institute, Baltimore, 1953, pp. 818-830.

[9] D.B. Spalding, The combustion of liquid fuels, in: 4th International Symposium on combustion, The Combustion Institute, Baltimore, 1953, pp. 847-864.

[10] C.K. Law, Unsteady droplet combustion with droplet heating, Combustion and Flame, 26 (1976) 17-22.

[11] C.K. Law, W.A. Sirignano, Unsteady droplet combustion with droplet heating--II: Conduction limit, Combustion and Flame, 28 (1977) 175-186.

[12] B. Abramzon, W.A. Sirignano, Droplet vaporization model for spray combustion calculations, International Journal of Heat and Mass Transfer, 32 (1989) 1605-1618.

[13] R.J. Haywood, R. Nafziger, M. Renksizbulut, Detailed examination of gas and liquid phase transient processes in convective droplet evaporation, Journal of Heat Transfer, 111 (1989) 495-502.

[14] C.H. Chiang, M.S. Raju, W.A. Sirignano, Numerical analysis of convecting, vaporizing fuel droplet with variable properties, International Journal of Heat and Mass Transfer, 35 (1992) 1307-1324.

[15] C.M. Megaridis, Comparison between experimental measurements and numerical predictions of internal temperature distributions of a droplet vaporizing under high-temperature convective conditions, Combustion and Flame, 93 (1993) 287-302.

[16] S.C. Wong, A.C. Lin, Internal temperature distributions of droplets vaporizing in high-temperature convective flows, Journal of Fluid Mechanics, 237 (1992) 671-687.

[17] A.T. Shih, C.M. Megaridis, Suspended droplet evaporation modeling in a laminar convective environment, Combustion and Flame, 102 (1995) 256-270.

[18] J.C. Lasheras, A.C. Fernandez-Pello, F.L. Dryer, Experimental observations on the disruptive combustion of free droplets of multicomponent fuels, Combustion science and technology, 22 (1980) 195-209.

[19] C.K. Law, Multicomponent droplet combustion with rapid internal mixing, Combustion and Flame, 26 (1976) 219-233.

[20] C.K. Law, Internal boiling and superheating in vaporizing multicomponent droplets, AIChE Journal, 24 (1978) 626-632.

[21] C. Maqua, G. Castanet, F. Lemoine, Bicomponent droplets evaporation: Temperature measurements and modelling, Fuel, 87 (2008) 2932-2942.

[22] S.S. Sazhin, A. Elwardany, P.A. Krutitskii, G. Castanet, F. Lemoine, E.M. Sazhina, M.R. Heikal, A simplified model for bi-component droplet heating and evaporation, International Journal of Heat and Mass Transfer, 53 (2010) 4495-4505.

[23] C.M. Megaridis, W.A. Sirignano, Numerical modeling of a vaporizing multicomponent droplet, Symposium (International) on Combustion, 23 (1990) 1413-1421.

[24] C.M. Megaridis, W.A. Sirignano, Multicomponent droplet vaporization in a laminar convective environment, Combustion Science and Technology, 87 (1993) 27-44.

[25] C.M. Megaridis, Liquid-Phase Variable Property Effects in Multicomponent Droplet Convective Evaporation, Combustion Science and Technology, 92 (1993) 291 - 311.

[26] H. Liu, E.J. Lavernia, R.H. Rangel, Numerical simulation of substrate impact and freezing of droplets in plasma spray processes, Journal of Physics D: Applied Physics, 26 (1993) 1900-1908.

[27] M. Pasandideh-Fard, R. Bhola, S. Chandra, J. Mostaghimi, Deposition of tin droplets on a steel plate: simulations and experiments, International Journal of Heat and Mass Transfer, 41 (1998) 2929-2945.

[28] L.L. Zheng, H. Zhang, An adaptive level set method for moving-boundary problems: Application to droplet spreading and solidification, Numerical Heat Transfer Part B-Fundamentals, 37 (2000) 437-454.

[29] M. Pasandideh-Fard, S. Chandra, J. Mostaghimi, A three-dimensional model of droplet impact and solidification, International Journal of Heat and Mass Transfer, 45 (2002) 2229-2242.

[30] R. Ghafouri-Azar, S. Shakeri, S. Chandra, J. Mostaghimi, Interactions between molten metal droplets impinging on a solid surface, International Journal of Heat and Mass Transfer, 46 (2003) 1395-1407.

[31] D.J.E. Harvie, D.F. Fletcher, A hydrodynamic and thermodynamic simulation of droplet impacts on hot surfaces, Part II: validation and applications, International Journal of Heat and Mass Transfer, 44 (2001) 2643-2659.

[32] D.J.E. Harvie, D.F. Fletcher, A hydrodynamic and thermodynamic simulation of droplet impacts on hot surfaces, Part I: theoretical model, International Journal of Heat and Mass Transfer, 44 (2001) 2633-2642.

[33] N. Nikolopoulos, A. Theodorakakos, G. Bergeles, A numerical investigation of the evaporation process of a liquid droplet impinging onto a hot substrate, International Journal of Heat and Mass Transfer, 50 (2007) 303-319.

[34] G. Strotos, M. Gavaises, A. Theodorakakos, G. Bergeles, Numerical investigation on the evaporation of droplets depositing on heated surfaces at low Weber numbers, International Journal of Heat and Mass Transfer, 51 (2008) 1516-1529.

[35] G. Strotos, M. Gavaises, A. Theodorakakos, G. Bergeles, Numerical investigation of the cooling effectiveness of a droplet impinging on a heated surface, International Journal of Heat and Mass Transfer, 51 (2008) 4728-4742.

[36] G. Strotos, M. Gavaises, A. Theodorakakos, G. Bergeles, Evaporation of a suspended multicomponent droplet under convective conditions, in: ICHMT, Marrakech, Morocco, 2008.

[37] G. Strotos, M. Gavaises, A. Theodorakakos, G. Bergeles, Influence of species concentration on the evaporation of suspended multicomponent droplets, in: ILASS 2008, Como Lake, Italy, 2008.

[38] C.W. Hirt, B.D. Nichols, Volume of Fluid (Vof) Method for the Dynamics of Free Boundaries, Journal of Computational Physics, 39 (1981) 201-225.

[39] O. Ubbink, R.I. Issa, A method for capturing sharp fluid interfaces on arbitrary meshes, Journal of Computational Physics, 153 (1999) 26-50.

[40] J.U. Brackbill, D.B. Kothe, C. Zemach, A continuum method for modeling surface tension, Journal of Computational Physics, 100 (1992) 335-354.

[41] A. Theodorakakos, G. Bergeles, Simulation of sharp gas-liquid interface using VOF method and adaptive grid local refinement around the interface, International Journal for Numerical Methods in Fluids, 45 (2004) 421-439.

[42] N. Nikolopoulos, A. Theodorakakos, G. Bergeles, Normal impingement of a droplet onto a wall film: a numerical investigation, International Journal of Heat and Fluid Flow, 26 (2005) 119-132.

[43] R.H. Perry, D.W. Green, Perry's Chemical Engineers' Handbook, 7th ed., McGraw-Hill, 1997.

[44] B.E. Poling, J.M. Prausnitz, J.P. O'Connell, Properties of Gases and Liquids (5th Edition), in, McGraw-Hill, 2001.

[45] Fluid_Research_Company, Manual on the GFS CFD code, in, 2002 , www.fluid-research.com.

[46] N. Nikolopoulos, A. Theodorakakos, G. Bergeles, Three-dimensional numerical investigation of a droplet impinging normally onto a wall film, Journal of Computational Physics, 225 (2007) 322-341.

[47] N. Nikolopoulos, A. Theodorakakos, G. Bergeles, Off-centre binary collision of droplets: A numerical investigation, International Journal of Heat and Mass Transfer, 52 (2009) 4160-4174.

[48] N. Nikolopoulos, K.-S. Nikas, G. Bergeles, A numerical investigation of central binary collision of droplets, Computers & Fluids, 38 (2009) 1191-1202.

[49] G. Strotos, N. Nikolopoulos, K.-S. Nikas, A parametric numerical study of the head-on collision behavior of droplets, Atomization and Sprays, 20 (2010) 191-209.

[50] M.E. Ranz , W.R. Marshall, Evaporation from drops: Part I, Chemical Engineering Progress, 48 (1952) 141-146.

[51] A. Daïf, M. Bouaziz, X. Chesneau, A. Ali Cherif, Comparison of multicomponent fuel droplet vaporization experiments in forced convection with the Sirignano model, Experimental Thermal and Fluid Science, 18 (1999) 282-290.

[52] R.H. Magarvey, R.L. Bishop, Transition ranges for three dimensional wakes, Can. j. Phys., 39 (1961) 1418-1422.

[53] J.-S. Wu, G.M. Faeth, Sphere wakes in still surroundings at intermediate Reynolds numbers, AAIA J., 31 (1993) 1448-1455.

[54] D.J. Torres, P.J. O'Rourke, A.A. Amsden, Efficient multicomponent fuel algorithm, Combustion Theory and Modelling, 7 (2003) 67-86.

[55] Y. Zeng, C.F. Lee, A model for multicomponent spray vaporization in a high-pressure and high-temperature environment, Journal of Engineering for Gas Turbines and Power, 124 (2002) 717-724.

[56] A. Ozturk, B.M. Cetegen, Modeling of plasma assisted formation of precipitates in zirconium containing liquid precursor droplets, Materials Science and Engineering A, 384 (2004) 331-351.

[57] I. Gökalp, C. Chauveau, H. Berrekam, N.A. Ramos-Arroyo, Vaporization of miscible binary fuel droplets under laminar and turbulent convective conditions, Atomization and Sprays, 4 (1994) 661-676.

[58] S. Taneda, Experimental Investigation of the Wake behind a Sphere at Low Reynolds Numbers, J. Phys. Soc. Japan, 11 (1956) 1104-1108.

[59] S. Prakash, W.A. Sirignano, Liquid fuel droplet heating with internal circulation, International Journal of Heat and Mass Transfer, 21 (1978) 885-895.

[60] S. Prakash, W.A. Sirignano, Theory of convective droplet vaporization with unsteady heat transfer in the circulating liquid phase, International Journal of Heat and Mass Transfer, 23 (1980) 253-268.

[61] G.M. Faeth, Current status of droplet and liquid combustion, Progress in Energy and Combustion Science, 3 (1977) 191-224.

Table 1: Experimental conditions

case	n-heptane % vol	d_0 [mm]	$T_{d,0}$ [K]	T_∞ [K]	u_∞ [m/s]	Re_0	t_{C10} [s]	FR_0
e1	100.0%	1.052	300	356	3.20	159	19.278	1.00
e2	74.0%	1.334	294	348	3.10	203	35.757	1.50
e3	63.5%	1.042	292	341	3.36	178	29.291	0.93
e4	43.0%	1.008	292	342	3.36	171	27.137	0.90
e5	21.3%	1.486	294	348	3.10	226	42.406	1.82
e6	0.0%	1.386	315	348	3.10	210	37.986	1.67

Table 2: Numerical conditions for the reference case.

n-heptane % in mass	75%	u_∞ [m/s]	3.2
d_0 [mm]	1.0	Re_0	155
$T_{d,0}$ [K]	300	FR_0	0.94
T_∞ [K]	350	t_{C10} [s]	21.041

Table 3: Numerical conditions for the parametric investigation

case name	less volatile	more volatile	Y_0	d_0 [mm]	T_∞ [K]	Re_0	FR_0	t_{C10} [s]
ref	C10	C7	0.75	1.0	350	155	0.94	21.041
C7 0%			0					
C7 25%			0.25					
C7 50%			0.5					
C7 100%			1					
T=400K					400	123	0.97	7.5758
T=450K					450	101	0.99	4.4975
d=0.2mm				0.2		31	0.08	1.534
d =0.1mm				0.1		16	0.03	0.4769
C10-C6		C6	0.75					
C10-C8		C8	0.75					
C10-C9		C9	0.75					
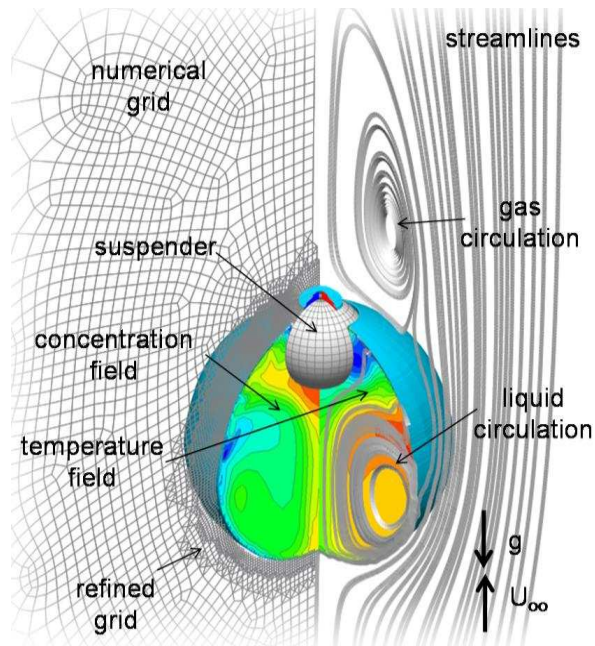
Fig. 1: A three-dimensional representation of one of the cases simulated. The numerical grid, selected streamlines, temperature and concentration fields inside the droplet are shown.
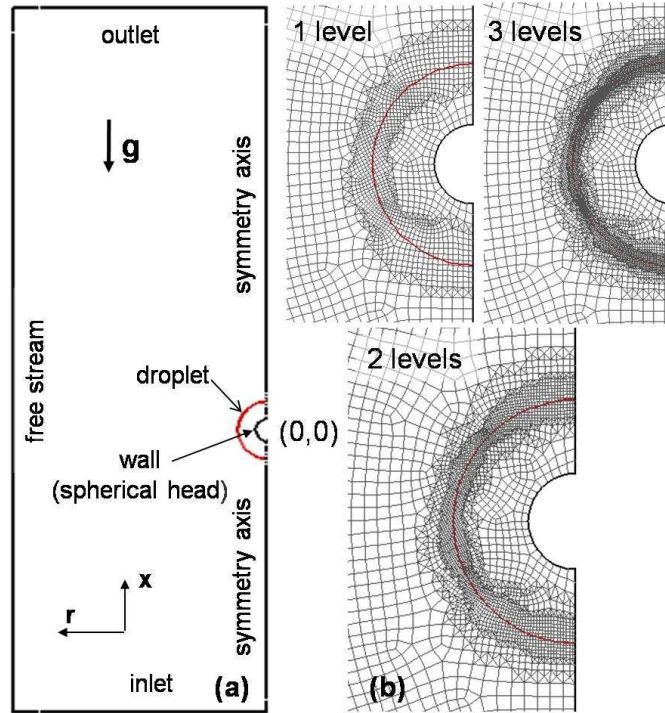
Fig. 2: (a) Computational domain and boundary conditions employed and (b) detail of the numerical grid around the liquid-gas interface using one-, two- and three-levels of adaptive local grid refinement.
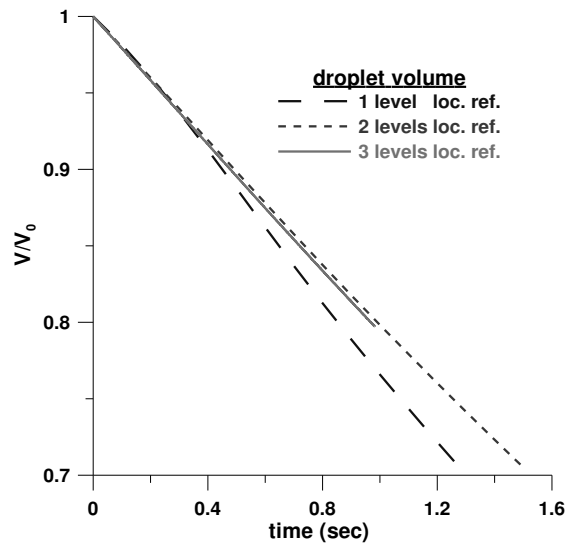
Fig. 3: Temporal evolution of droplet's non-dimensional volume for the reference case using one-, two- and three-levels of local grid refinement.
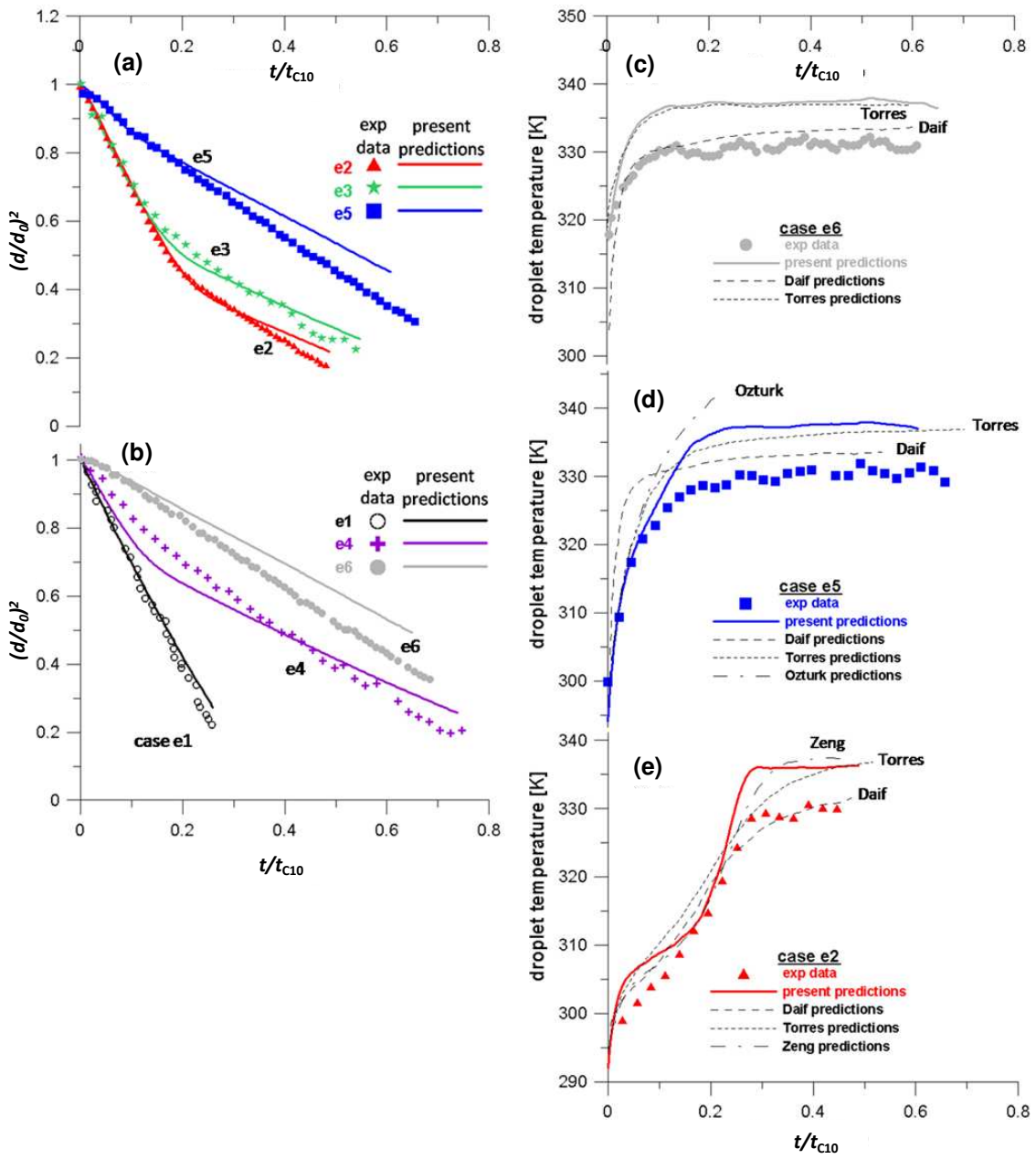
Fig. 4: (a,b) Numerical prediction of the temporal evolution of droplet size and (c,d,e) mean droplet temperature.
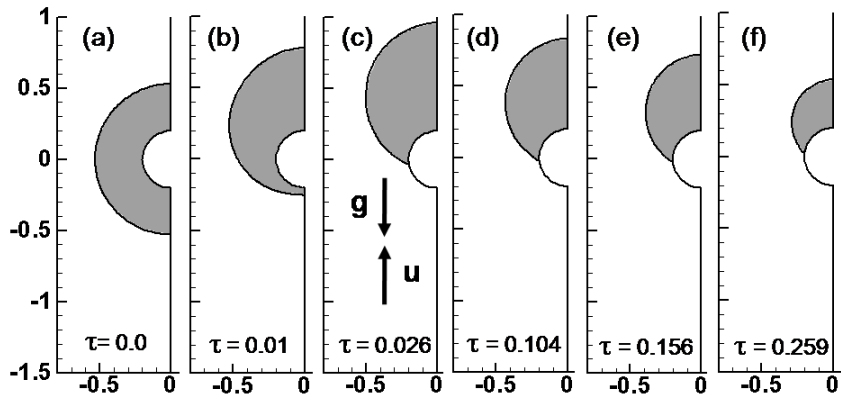
Fig. 5: Droplet movement and equilibrium position for case e1.
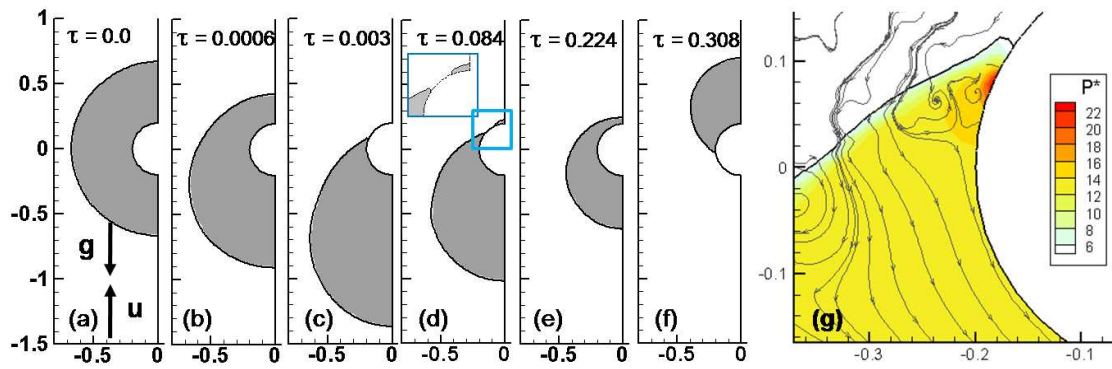
Fig. 6: Droplet equilibrium position and meniscus creation for case e2.
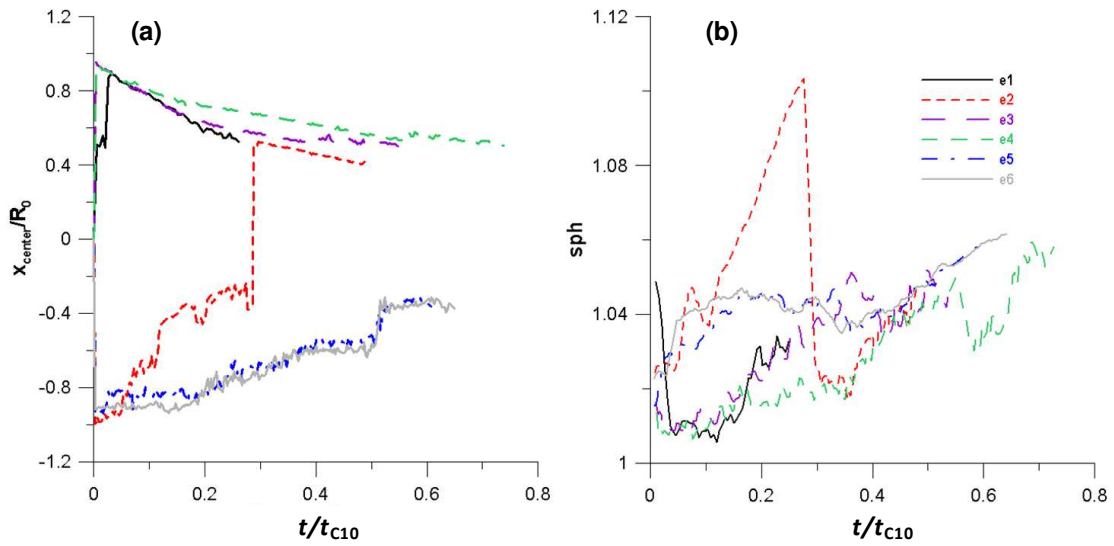
Fig. 7: (a) Predicted temporal evolution of the center of volume of the droplet and (b) deviation from the spherical shape.
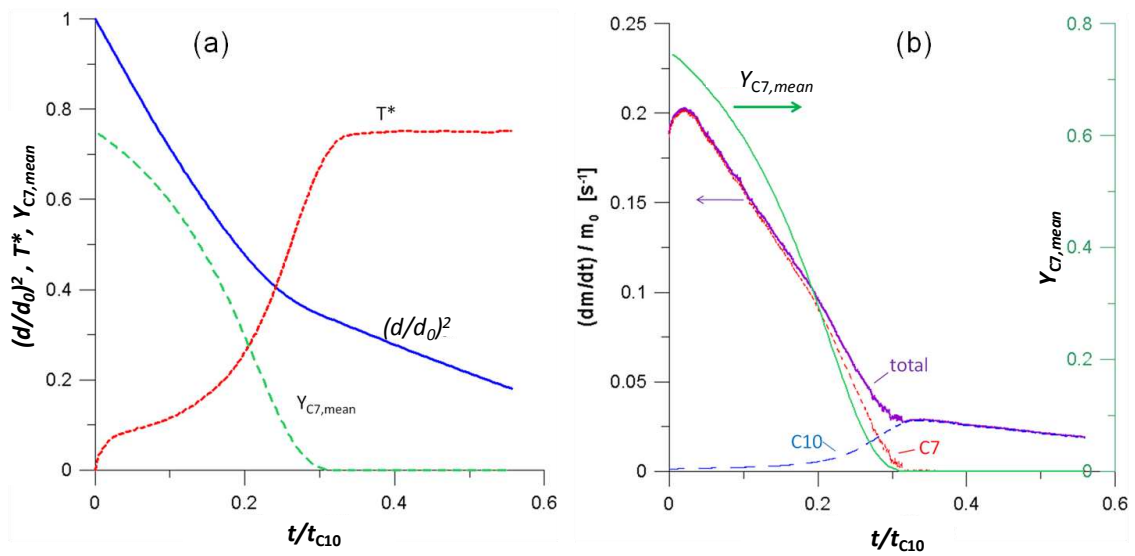
Fig. 8: (a) Predicted temporal evolution of droplet's size and droplet's mean temperature and (b) predicted evaporation rate of each species and total evaporation rate. In both figures the concentration of n-heptane is also presented.
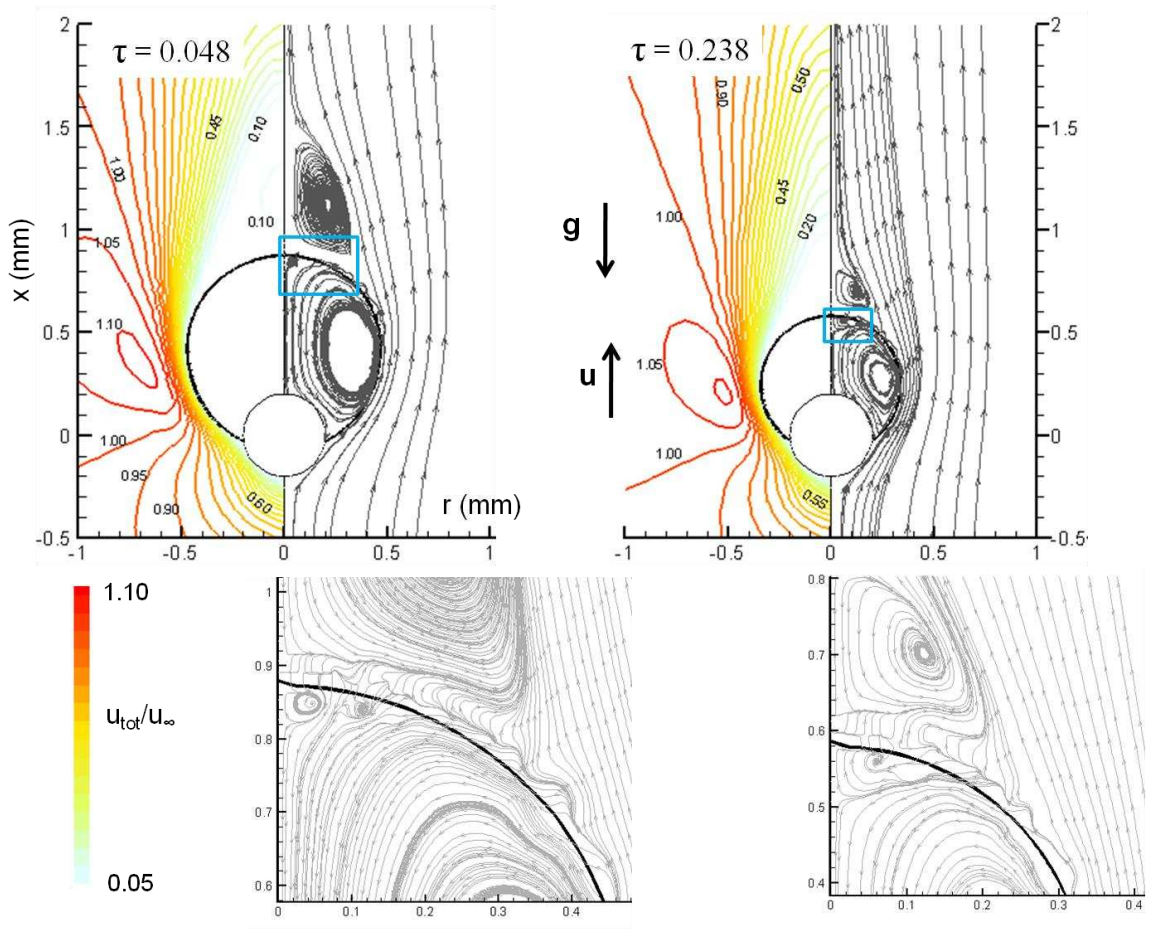
Fig. 9: Total velocity magnitude (left-hand-side) and streamlines (right-hand-side) for the reference case.
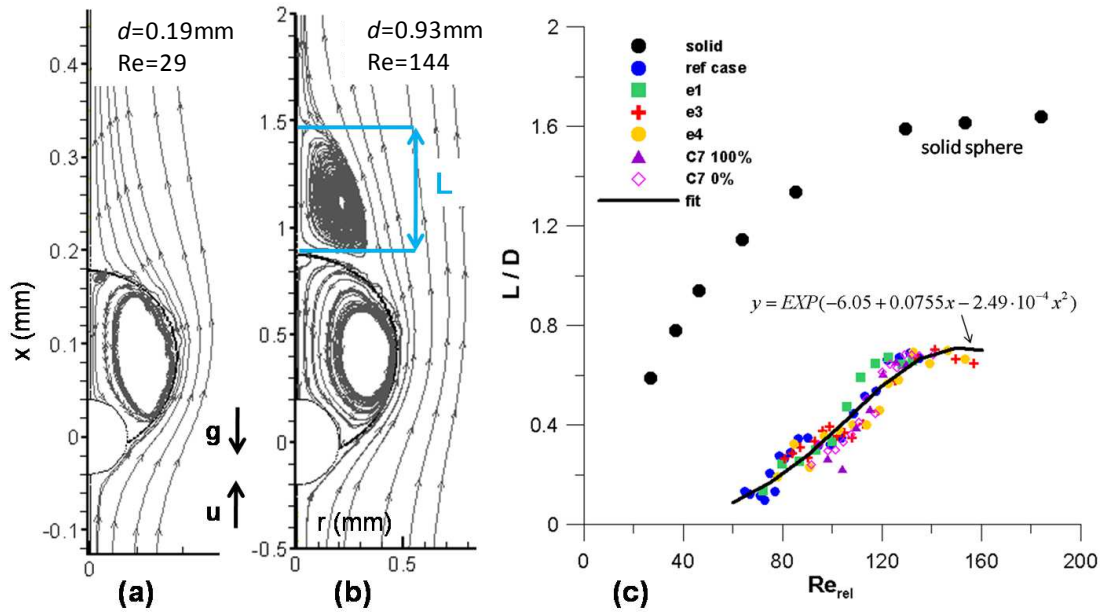
Fig. 10: (a) Streamlines for low Reynolds number, (b) streamlines for higher Reynolds number and (c) dependence of the recirculation length with Re number.
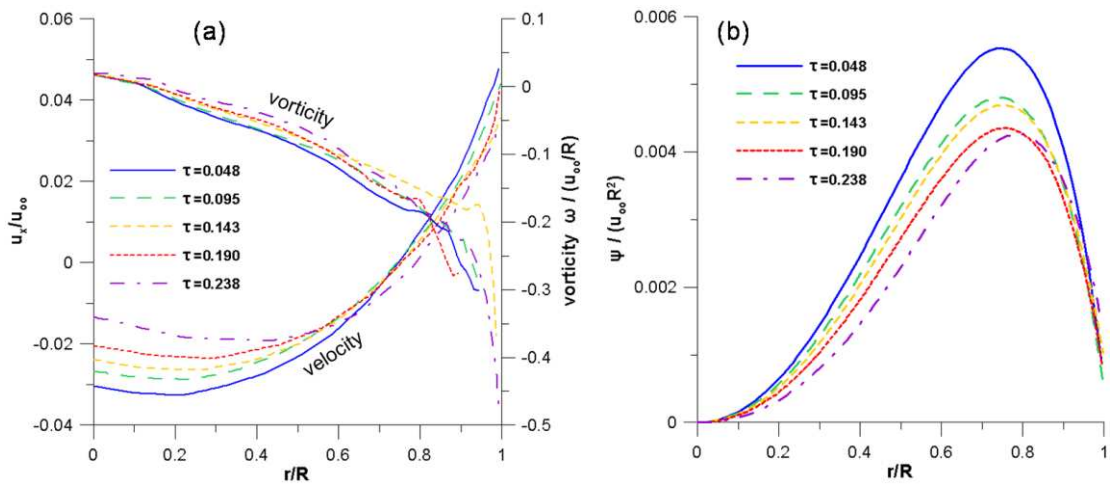
Fig. 11: Radial distribution of (a) dimensionless velocity and dimensionless vorticity and (b) dimensionless stream-function through the vortex centre
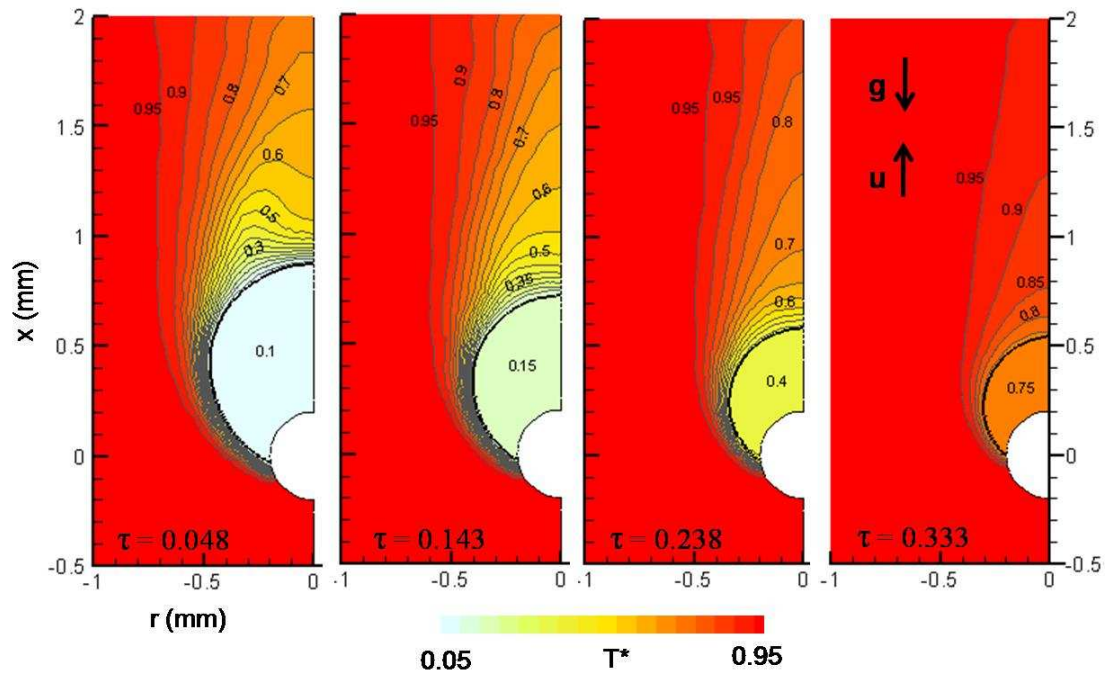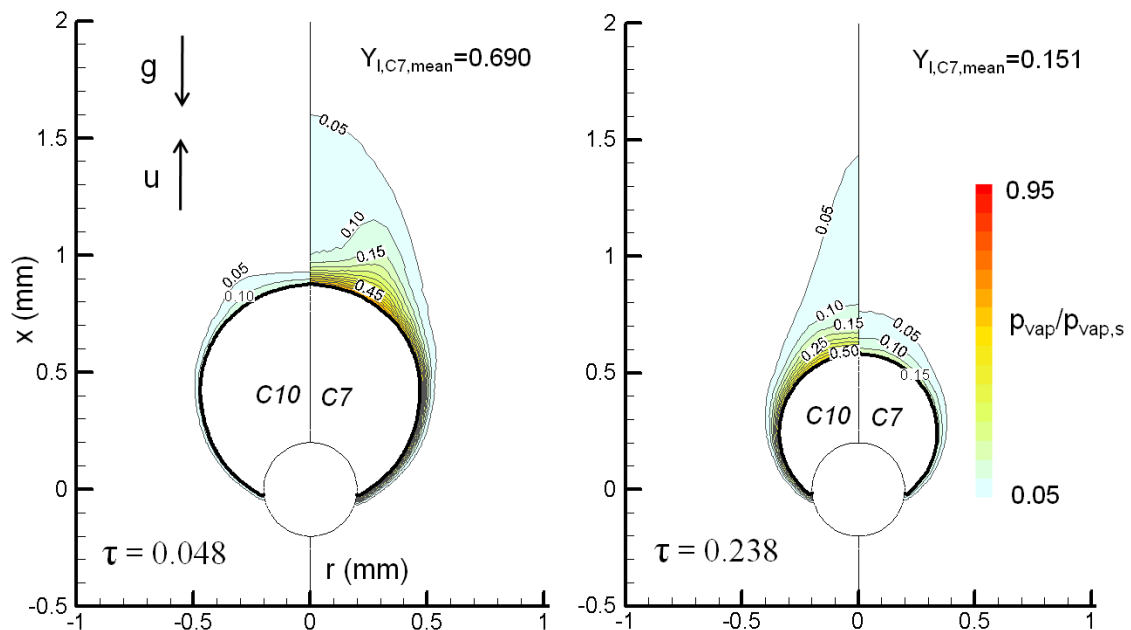
Fig. 12: Non-dimensional temperature field T^* for the reference case.

Fig. 13: Vapor pressure field non-dimensionalised with saturation pressure for each species for n-decane (left part) and n-heptane (right part) for the reference case at two time instances of τ=0.048 and τ=0.238.
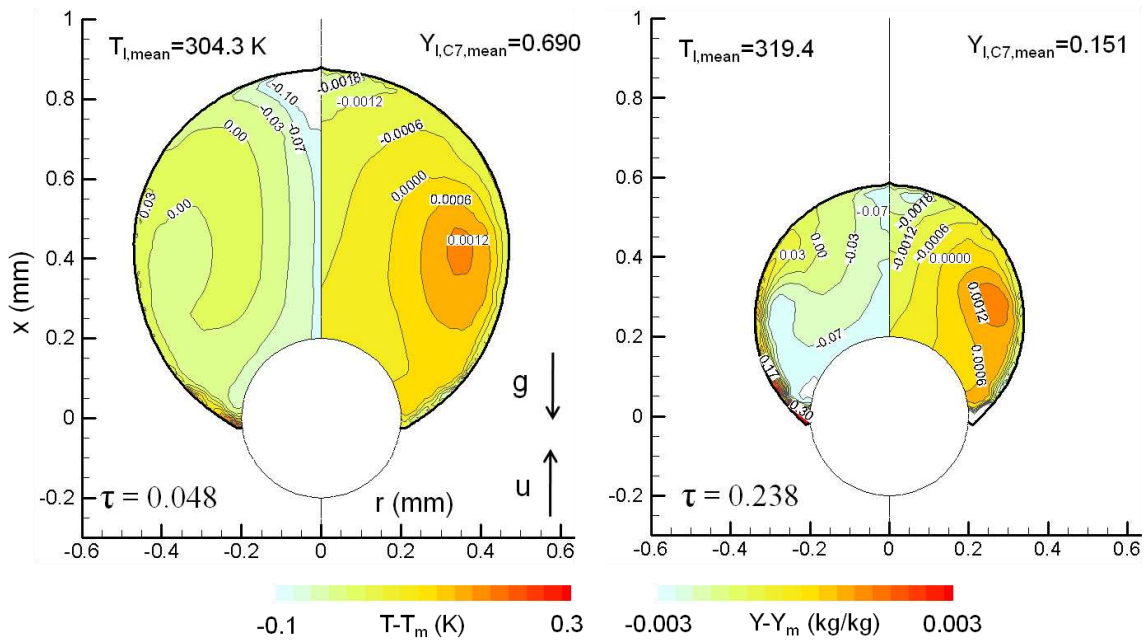
Fig. 14: Temperature field (left-hand-side) and concentration field (right-hand-side) inside the liquid phase for the reference case at two time instances of τ=0.048 and τ=0.238.
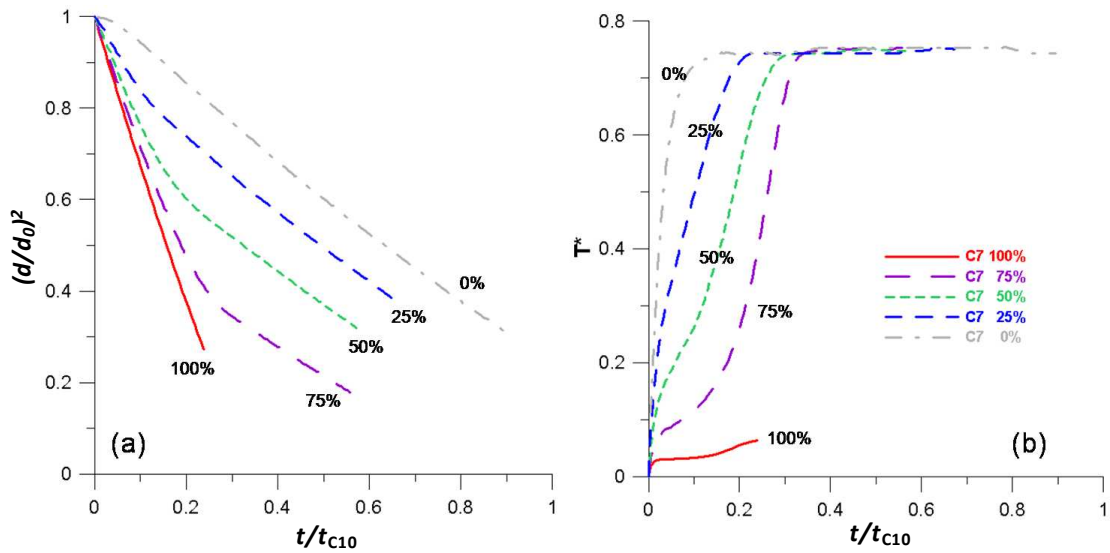

Fig. 15: Predicted temporal evolution of (a) droplet's size and (b) droplet's mean dimensionless temperature, showing the influence of the initial concentration in n-heptane.
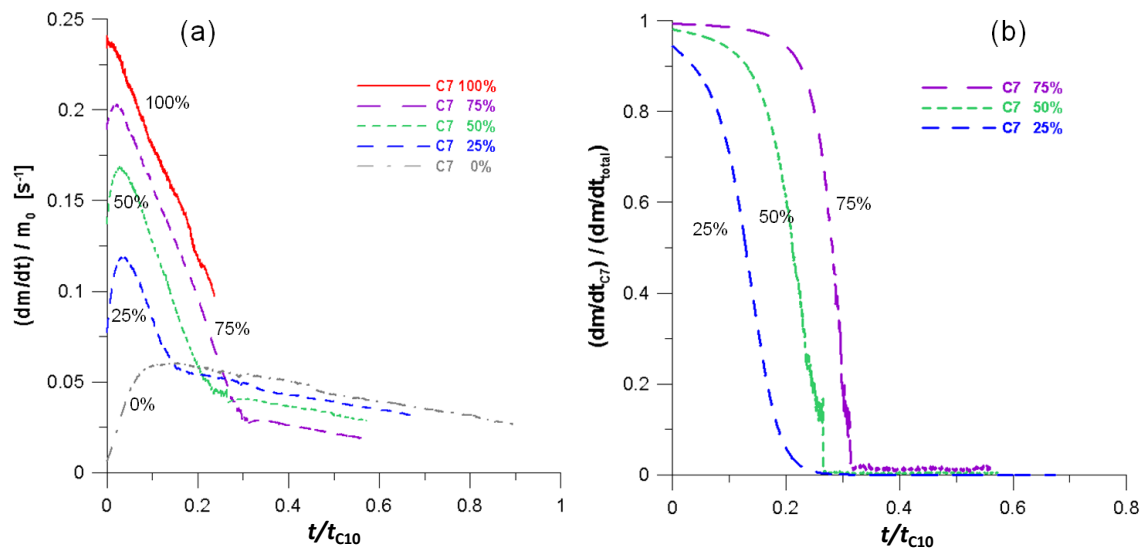
41

Fig. 16: Temporal evolution of (a) total evaporation rate and (b) contribution of the volatile n-heptane to the total evaporation rate.
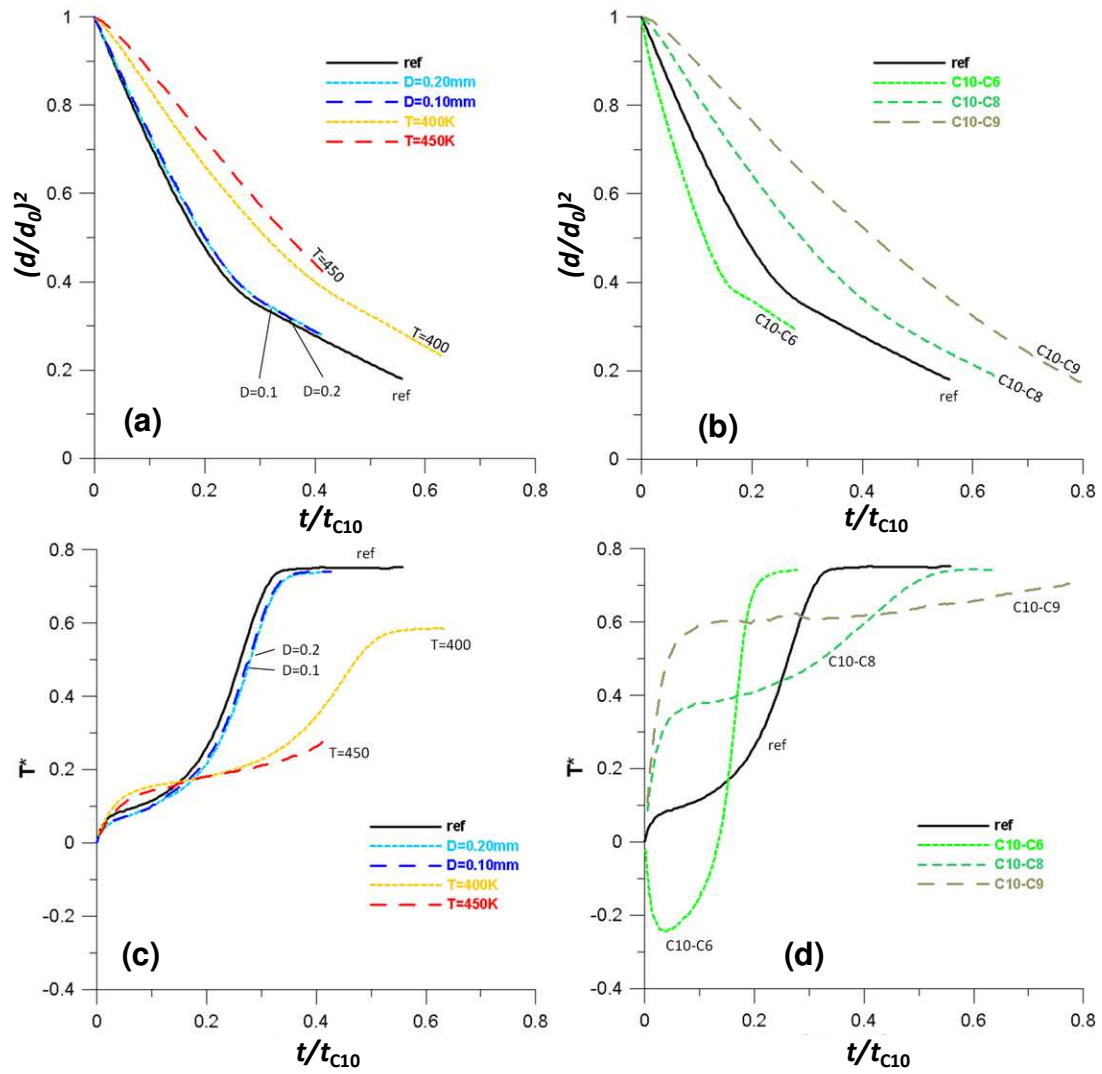
Fig. 17: Predicted temporal evolution of dimensionless droplet squared diameter (upper part a, b) and droplet's mean temperature (lower part c, d), showing the influence of the droplet size, gas phase temperature (left part a,c) and species volatility difference (right part b, d).

.